

Generative Inversion for Property-Targeted Materials Design: Application to Shape Memory Alloys

Cheng Li^{a,1}, Pengfei Dang^{a,1}, Yuehui Xian^a, Yumei Zhou^{*a}, Bofeng Shi^a, Xiangdong Ding^{*a}, Jun Sun^a, Dezhen Xue^{*a}

^aState Key Laboratory for Mechanical Behavior of Materials, Xi'an Jiaotong University, Xi'an 710049, China

Abstract

The design of shape memory alloys (SMAs) with high transformation temperatures and large mechanical work output remains a longstanding challenge in functional materials engineering. Here, we introduce a data-driven framework based on generative adversarial network (GAN) inversion for the inverse design of high-performance SMAs. By coupling a pretrained GAN with a property prediction model, we perform gradient-based latent space optimization to directly generate candidate alloy compositions and processing parameters that satisfy user-defined property targets. The framework is experimentally validated through the synthesis and characterization of five NiTi-based SMAs. Among them, the $\text{Ni}_{49.8}\text{Ti}_{26.4}\text{Hf}_{18.6}\text{Zr}_{5.2}$ alloy achieves a high transformation temperature of 404 °C, a large mechanical work output of 9.9 J/cm³, a transformation enthalpy of 43 J/g, and a thermal hysteresis of 29 °C, outperforming existing NiTi alloys. The enhanced performance is attributed to a pronounced transformation volume change and a finely dispersed of Ti₂Ni-type precipitates, enabled by sluggish Zr and Hf diffusion, and semi-coherent interfaces with localized strain fields. This study demonstrates that GAN inversion offers an efficient and generalizable route for the property-targeted discovery of complex alloys.

Keywords: Inverse design, Generative adversarial networks (GANs), Shape memory alloys (SMAs), High-temperature actuation, Data-driven materials discovery

1. Introduction

Shape memory alloys (SMAs) are functional materials that undergo reversible martensite transformations, enabling them to recover large strains and perform work output in response to mechanical stimuli [1, 2]. They are widely employed in aerospace actuators, biomedical devices, and energy conversion systems [3, 4]. Ultra high temperature SMAs operating reliably above 300 °C with substantial mechanical work output are essential for mission-critical aerospace and nuclear systems, where conventional SMAs fail due to a phase transformation temperature limitation [5, 6]. The intricate interdependencies among composition, microstructure, and processing parameters create a high-dimensional optimization challenge for achieving the targeted combination of elevated transformation temperatures, large latent heat, low thermal hysteresis, and high work output [5, 7–9].

Conventional alloy design strategies, including empirical trial-and-error, thermodynamic modeling, and micromechanical simulations, have provided valuable insights but remain inherently constrained in their ability to efficiently explore high-dimensional, nonlinear design spaces. To overcome these limitations, recent advances in data-driven materials design have employed machine learning (ML) techniques to accelerate alloy discovery and optimization [10, 11]. In the context of SMAs, several studies have developed surrogate models to predict transformation temperatures or thermal hysteresis from compositional and processing descriptors, with some predictions successfully validated through experimental synthesis [1, 12–17]. For example, polynomial regression models informed by Landau theory have been used to predict transformation temperatures, and Bayesian optimization has guided the design of alloys with low hysteresis, large shape memory response, and high transformation enthalpy [18–24]. Predictive ML models have also been applied to the co-optimization of elastocaloric strength and stress hysteresis in elastocaloric alloys, demonstrating their utility for multi-

*Corresponding author

Email addresses: zhoyumei@xjtu.edu.cn (Yumei Zhou*), xuedezhen@xjtu.edu.cn (Dezhen Xue*)

¹The two authors contributed equally to this work.

objective materials design [25, 26].

Beyond forward property prediction, there is growing interest in inverse design strategies aimed at identifying input parameters that yield user-defined material properties [27–31]. Generative models, particularly variational autoencoders (VAE) [32] and generative adversarial networks (GAN) [33], have emerged as promising tools for this purpose in complex alloy systems, including high entropy alloys [34–37], magnesium alloys [38], titanium alloys [39, 40], aluminium alloys [41, 42], metallic glasses [43], dual-phase steel [44–47], Beryllium Alloys [48]. For instance, VAEs coupled with active learning have been used to identify high-entropy alloys (HEAs) with record-low thermal expansion [34], and GAN coupled with neural regression were used to design multi-principal-element alloys exhibiting record-high hardness [35]. In the context of SMAs, a conditional VAE framework has been developed to co-design composition and processing conditions. Notably, this approach enabled the generation of NiTi-based alloys tailored to match user-specified transformation property curves, with multiple designs successfully validated via experimental synthesis [49]. Inverse design methods mentioned above employing direct condition embedding face significant risks of mode collapse when trained on limited material datasets, mirroring the challenges observed in image-based generative models [50, 51].

In the present study, we introduce a generative inversion framework for the inverse design of high-performance SMAs based on an implicit condition fusion mechanism driven by gradient-based optimization. Our method integrates a pretrained GAN, which captures the joint distribution of alloy compositions and processing parameters, with a property prediction model trained to estimate transformation characteristics. By performing gradient-based optimization in the latent space of the GAN, the framework enables a direct and differentiable mapping from property space to design space. This allows for the rapid, interpretable generation of candidate alloy designs that satisfy user-defined targets, such as transformation temperature and mechanical work output. Although demonstrated here on SMAs, the framework is generalizable and can be extended to a broad range of material systems, including high-entropy alloys and ceramics.

2. Design Strategy

2.1. Overview of the Inverse Design Framework

To enable the inverse design of SMAs with tailored transformation temperatures and mechanical work out-

puts, we employ a generative inversion [52, 53] framework based on a pretrained GAN. The key idea is to map user-specified property targets back to alloy compositions and processing parameters through gradient-based optimization in the latent space of the GAN.

This framework, as shown in Figure 1, comprises four main components: a generator trained to produce realistic alloy designs (i.e., composition and processing), a property predictor that estimates thermo-mechanical responses such as martensite start temperature (M_s) and mechanical work output, a differentiable loss function quantifies the difference between candidate samples properties and target properties, and an Adam optimizer updates the latent code \mathbf{z} to minimize the loss. By coupling generative modeling with property prediction, the framework can achieve reverse design and random generation by sampling \mathbf{z} without optimization. For inverse design, the latent vector of the GAN is iteratively optimized to minimize the loss function, producing candidates that progressively satisfy user-defined objectives.

2.2. Latent Space Optimization for Property-Targeted Design

Generative Model and Surrogate Predictor. We first train a Wasserstein GAN with gradient penalty (WGAN-GP) [53, 54]. The generator $G: \mathbb{R}^d \rightarrow \mathbb{R}^n$, which maps a latent vector $\mathbf{z} \in \mathbb{R}^d$ to a design vector $\mathbf{x} = G(\mathbf{z}) \in \mathbb{R}^n$. Each design vector \mathbf{x} includes both alloy composition $\mathbf{c} \in \mathbb{R}^{n_c}$ and processing parameters $\mathbf{p} \in \mathbb{R}^{n_p}$, i.e., $\mathbf{x} = (\mathbf{c}, \mathbf{p})$. The discriminator $D: \mathbb{R}^n \rightarrow \mathbb{R}$, outputs scalar scores for authenticity of vector \mathbf{x} . Specifically, d , n , n_c , and n_p are set to 10, 19, 10, and 9, respectively. The WGAN-GP loss functions are defined as:

$$\mathcal{L}_D = E_{\tilde{\mathbf{x}} \sim P_g} [D(\tilde{\mathbf{x}})] - E_{\mathbf{x} \sim P_r} [D(\mathbf{x})] + \lambda \mathcal{P} \quad (1)$$

$$\mathcal{P} = E_{\tilde{\mathbf{x}} \sim P_g} [(\|\nabla_{\tilde{\mathbf{x}}} D(\tilde{\mathbf{x}})\|_2 - 1)^2] \quad (2)$$

$$\mathcal{L}_G = -E_{\tilde{\mathbf{x}} \sim P_g} [D(\tilde{\mathbf{x}})] \quad (3)$$

where P_r is the real data distribution, P_g is the generated data distribution, and $\tilde{\mathbf{x}}$ denotes random interpolates between real and generated samples. The gradient penalty term \mathcal{P} (weighted by $\lambda=10$) enforces Lipschitz continuity. The training protocol implements asynchronous updates with distinct learning rates for the G and D, 0.0002 and 0.0008, respectively. This approach mitigates mode collapse and improves gradient stability compared to conventional GANs.

In parallel, a artificial neural network (ANN) surrogate model $f: \mathbb{R}^n \rightarrow \mathbb{R}^m$ is trained to predict material properties $\mathbf{y} \in \mathbb{R}^m$, such as M_s and mechanical work output (the

product of stress and recoverable phase transformation strain). The predictor loss functions are defined as:

$$\mathcal{L}_{\text{surrogate}} = \frac{1}{N} \sum_{i=1}^N \|f(\mathbf{x}_i) - \mathbf{y}_i\|^2 + \beta \mathcal{L}_{\text{knowledge}}, \quad (4)$$

where $(\mathbf{x}_i, \mathbf{y}_i)$ are training pairs, $\mathcal{L}_{\text{knowledge}}$ is domain-informed constraint derived from our prior studies [14], β is weighting coefficient for the domain-informed constraint, set to 5 in this work. This loss function maintains data fidelity while enforcing physical consistency. The WGAN-GP and predictor are trained using a dataset of known composition–processing–properties pairs, totaling 750 data points, derived from experimental measurements in our laboratory and literature data [6, 55–85]. The parameter settings for WGAN-GP and surrogate models are detailed in the Supplementary Information Table S1 and S2.

Inverse Design via Latent Space Optimization. Given a target property vector $\mathbf{y}_t \in \mathbb{R}^m$, we aim to find a latent code \mathbf{z}^* such that the generated design $\mathbf{x}^* = G(\mathbf{z}^*)$ yields predicted properties $\hat{\mathbf{y}} = f(\mathbf{x}^*)$ that match the target. This leads to the optimization problem:

$$\mathbf{z}^* = \arg \min_{\mathbf{z}} \mathcal{L}(\mathbf{z}) = \arg \min_{\mathbf{z}} \|f(G(\mathbf{z})) - \mathbf{y}_t\|^2. \quad (5)$$

Optimization Procedure. This loss is minimized using gradient-based methods such as the Adam optimizer, with updates of the form:

$$\mathbf{z}_{k+1} = \mathbf{z}_k - \eta \cdot \nabla_{\mathbf{z}} \mathcal{L}(\mathbf{z}_k), \quad (6)$$

where η is the learning rate, set to 0.04 in this work. Optimization is initialized with a random latent vector $\mathbf{z}_0 \sim \mathcal{N}(0, I)$ and proceeds until the predicted property satisfies a convergence criterion:

$$\|f(G(\mathbf{z}^*)) - \mathbf{y}_t\| < \epsilon. \quad (7)$$

Final Design Selection. Once converged, the optimized latent vector \mathbf{z}^* is decoded to obtain the final alloy design:

$$\mathbf{x}^* = G(\mathbf{z}^*) = (\mathbf{c}^*, \mathbf{p}^*), \quad \hat{\mathbf{y}}^* = f(\mathbf{x}^*) \approx \mathbf{y}_t. \quad (8)$$

The final design \mathbf{x}^* can then be validated through high-fidelity simulations or experimental synthesis to confirm its thermo-mechanical performance. A detailed pseudocode outlining the GAN inversion steps is provided in the Supplementary Information (Table S3). This approach enables efficient, interpretable, and experimentally accessible alloy design across coupled compositional, processing, and property spaces.

2.3. Experimental

New alloys were synthesized according to the chemically optimized compositions derived from our design strategy. High-purity elements (99.9 at.% Ti, Ni, and Cu; 99.5 at.% Hf and Zr) along with a Ti-60Ta wt.% master alloy (XI'AN Rare Metal Materials Institute Co. Ltd) were arc-melted under argon atmosphere using a water-cooled copper crucible. To ensure compositional homogeneity, each ingot was remelted six times followed by flipping between melts. These alloys were then heat treated according to the recommended temperature, time, and cooling method of the GAN inversion.

Transformation characteristics were evaluated using differential scanning calorimetry (DSC; Netzsch 214) with heating/cooling rates of 10 °C/min. Shape memory properties were characterized through uniaxial constant-stress thermal cycling tests performed on dog-bone specimens using a uTS tensile testing system (10 °C/min). Temperature monitoring was achieved via a welded K-type thermocouple, while strain evolution was tracked using digital image correlation (DIC) with a stochastic white speckle pattern applied to the gauge section.

Phase analysis was conducted via transmission wide-angle X-ray diffraction (XRD; NANOPIX-WE system, Rigaku Co., Tokyo, Japan) employing a Mo rotating anode source ($\lambda=0.7093$ Å). Microstructural characterization was performed using a scanning electron microscopy (SEM; Zeiss sigma360) and a transmission electron microscopy (TEM; JEM F200) at 200 kV. TEM specimens were prepared by twin-jet electropolishing in a 10 vol% HClO₄ and 90 vol% CH₃OH electrolyte maintained at -20 °C.

3. Results and Discussion

3.1. Statistical Reconstruction Fidelity and Diversity Metrics of Generator

We first assess the capacity of pretrained GAN to replicate the complex, high-dimensional relationships between compositions, processing parameters, and their properties, as this represents a critical prerequisite for effective inverse design applications. We use diversity and falsity metrics to determine the optimal parameter state of the pretrained GAN, as shown in Supplementary Information (Figure S1).

To assess structural fidelity, we project both real and generated samples into a shared two-dimensional embedding using t-SNE (Figure 2a). Real samples are shown in orange and GAN-generated samples in blue. The high degree of overlap between the two distributions indicates that the generator learns a meaningful approximation of

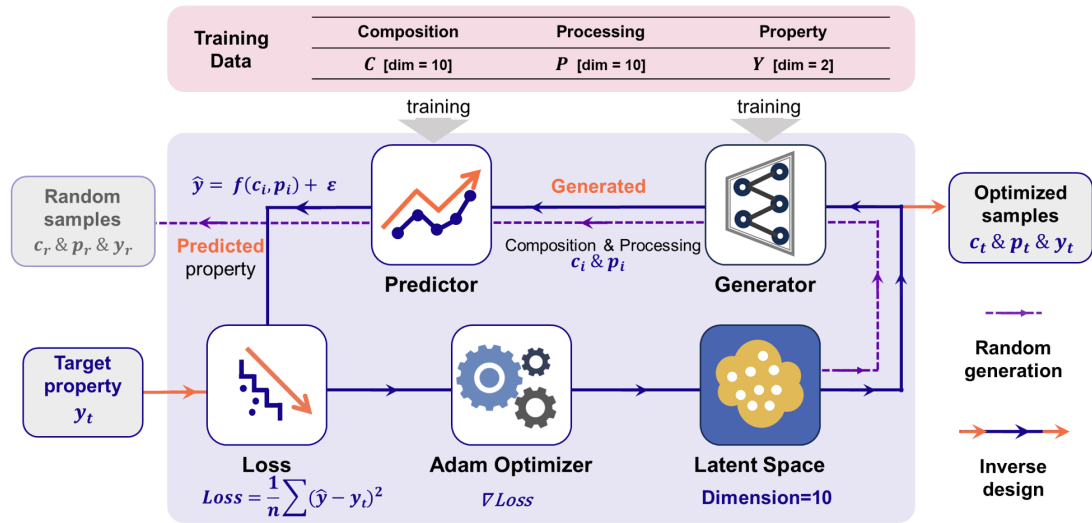


Figure 1: **Schematic of the GAN inversion framework for property-targeted inverse design of shape memory alloys.** The framework integrates a pretrained GAN with a supervised property predictor to enable inverse mapping from target performance to alloy design. For inverse design, a random latent vector \mathbf{z} is sampled from a 10-dimensional latent space and decoded by the generator to produce candidate design vectors $(\mathbf{c}_t, \mathbf{p}_t)$. The predictor estimates the corresponding properties $\hat{y} = f(\mathbf{c}_t, \mathbf{p}_t)$, and the discrepancy with the target property y_t is evaluated via a differentiable loss function. An Adam optimizer updates the latent code \mathbf{z} to minimize the loss, guiding the generator toward design candidates whose predicted properties approach y_t . The result is a set of optimized samples $(\mathbf{c}_t, \mathbf{p}_t, \hat{y}_t)$ that satisfy user-defined property objectives. The same framework can also be used for unconditional random generation by sampling \mathbf{z} without optimization.

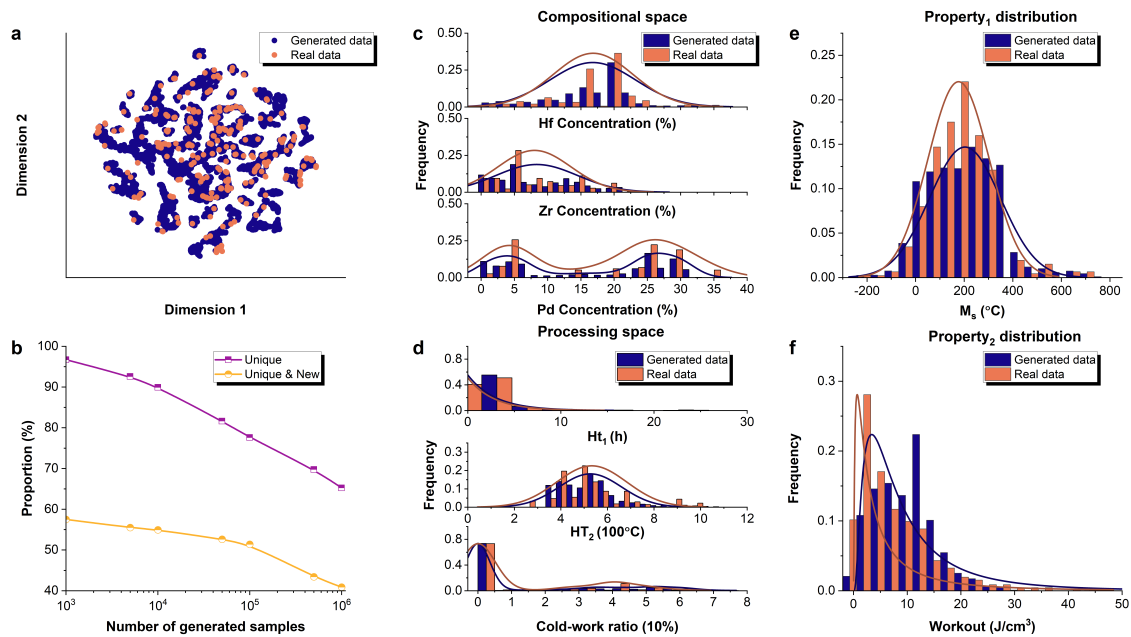


Figure 2: **Evaluation of the generative performance of the trained GAN model.** (a) t-SNE visualization of real (orange) and GAN-generated (blue) samples in compositional and processing parameters space, showing strong distributional overlap and indicating that the generator captures the underlying data manifold. (b) Diversity analysis of generated samples as a function of generation size. “Unique” and “Unique & New” score reflects the model’s ability to generate novel designs. Comparison of marginal distributions for key alloying elements (Hf, Zr, Pd) (c), processing parameters (primary heat treatment time, secondary heat treatment temperature, and cold-work ratio) (d), key material properties (M_s and workout) (e)–(f) between generated and real samples, demonstrating preservation of data features.

the underlying design manifold, preserving global and local structure in the composition–processing space.

We then assess the Unique and Unique & New metric of the generated samples (Figure 2b) based on cosine similarity. "Unique" refers to non-redundant samples and "Unique & New" are samples unique and not present in the training data. Although the fraction of both unique and unique & new shows moderate decay on scale, the generator maintains robust novelty retention, yielding 40 % unique and previously unseen samples even at 10^6 samples. This behavior reflects fundamental probability constraints, as sample volume increases, the likelihood of sampling similar latent space points rises proportionally, particularly in high-density distribution regions, consistent with state-of-the-art generative models [27].

Next, we examine whether the model reproduces the statistical characteristics of key design variables. Figure 2c compares the marginal distributions of representative alloying elements (Hf, Zr, and Pd) between real and generated data. The generator maintains the multimodal character and relative frequency of each composition feature, indicating a strong match to the empirical compositional priors. Similarly, Figure 2d shows that processing parameters such as primary heat treatment time, secondary heat treatment temperature, and cold-work ratio are faithfully reproduced.

Finally, we evaluate whether the generator can produce realistic property values based on surrogate property predictor, which maps design vectors to thermo-mechanical responses. On the held-out test set, the predictor achieves a coefficient of determination of R^2 of 0.90 and a Root Mean Square Error (RMSE) of 43.89 °C for M_s , and R^2 of 0.84 with an RMSE of 2.13 J/cm³ for mechanical work output. These results confirm the surrogate’s ability to learn the underlying elements-processing and property relationships with sufficient precision for guiding latent space optimization. Detailed error analyses are provided in the Supplementary Information (Figure S2–S4). Figure 2e–f compare the distributions of M_s and mechanical work output between generated and real samples. The generated data spans the full range of observed property values, from low to high M_s and from low to high actuation workout. Other distributions of elements and processing parameters between real and generated data are provided in the Supplementary Information (Figure S5 and S6). The above analysis reflects a desirable balance: the generator maintains high fidelity to the training data while also enabling exploration of novel designs beyond the observed dataset.

3.2. Latent Space Optimization Toward Targeted Thermo-Mechanical Properties

To evaluate capability of the proposed framework for inverse design, we examine two representative inverse design trajectories generated by GAN inversion: one targeting elevated M_s , and the other targeting increased mechanical work output. Figure 3a illustrates the op-

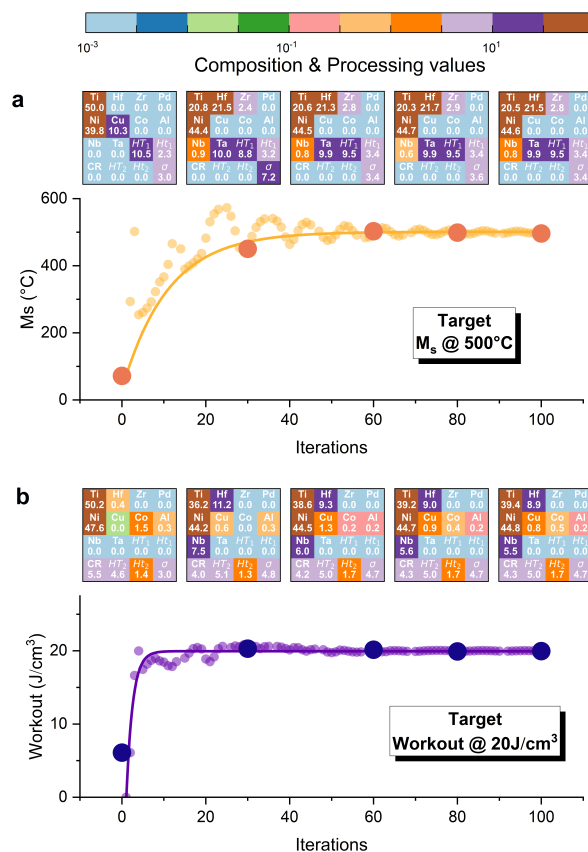


Figure 3: **Latent space optimization trajectories for property-targeted inverse design using GAN inversion.** (a) Optimization of M_s starting from a randomly initialized latent vector. Each point represents the predicted M_s from the surrogate model at a given iteration. The inversion process progressively shifts the design toward alloys predicted to exceed 500 °C in M_s . (b) Optimization targeting increased mechanical work output. As in panel (a), the inversion iteratively updates the latent vector to maximize predicted workout, approaching the specified target of 20 J/cm³. The curve traces the optimization path, and representative design snapshots reveal how compositional and processing features evolve to support enhanced performance.

timization of M_s beginning from a randomly sampled latent vector \mathbf{z}_0 . At each iteration, the generator produces a candidate design $\mathbf{x}_i = G(\mathbf{z}_i)$, which is evaluated by the surrogate model to predict the corresponding M_s . The curve shows a smooth, monotonic increase in predicted M_s , ultimately converging toward the target value of

500 °C. This behavior highlights the differentiability and directionality of the latent space, enabling efficient navigation toward high-temperature transformation regimes.

To gain insight into the underlying design evolution, five selected designs along the trajectory are visualized in terms of their compositional and processing attributes by heatmap. The heatmap values correspond to atomic percentages (for compositions) and scaled units (for processing variables), with full variable definitions provided in [the Supplementary Information \(Table S4\)](#). These heatmaps reveal systematic trends, such as increased Hf, Zr and Ta content or adjustments in heat treatment parameters, that correlate with rising M_s . [Figure 3b](#) shows a parallel optimization targeting mechanical workout. Starting again from a random initialization, the inversion trajectory drives the predicted workout toward a target of 20 J/cm³, with rapid improvement observed in the early stages. As in the temperature-targeting example, the evolving design vectors are visualized as composition–processing heatmaps. The optimization induces increases in elements and processing conditions known to support high actuation stress and strain recovery.

The observed trajectories demonstrate robust convergence behavior and physically interpretable design pathways, validating the capability of framework capability for targeted property optimization in shape memory alloys. These results establish the efficacy of framework in addressing inverse design challenges across complex, nonlinear, and multi-variable materials systems.

3.3. Targeted Property Control and Design Diversity through GAN Inversion

Here, we evaluate the ability of the framework to generate designs that are both precise, novel, and diverse in chemistry and processing space.

To assess precision, we perform conditional generation for a range of martensite start temperature (M_s) and mechanical work output targets. As shown in [Figure 4a–b](#), the predicted property distributions of generated samples are tightly centered around the specified targets, clearly shifted away from the broad baseline of the seed distribution. For example, M_s values generated for targets of 200, 400, and 500 °C exhibit increasing medians that align with their respective objectives. However, when targeting more extreme values (such as 500 °C), the variance becomes larger, reflecting reduced precision caused by limited training data in the high-temperature regime. Similar behavior is observed in the workout-targeted samples. While the medians consistently reach their objectives, the spread increases at higher target values.

To explore the latent dynamics of conditional generation, we apply principal component analysis (PCA) to the design vectors ([Figure 4c–d](#)). Compared to the dense cluster of initial seed points (navy), the generated samples exhibit distinct directional shifts depending on the targeted property. For instance, designs optimized for high M_s and high workout occupy different regions of the PCA space. These shifts indicate that the model learns to explore separable areas of the design manifold that correspond to different thermo-mechanical objectives, reflecting distinct chemical and processing strategies.

We further assess design diversity using histograms of alloying element count and processing complexity ([Figure 4e–f](#)). Alloys optimized for high mechanical work output tend to involve more elaborate processing protocols, often incorporating two or more distinct heat treatments. In contrast, high M_s designs are more likely to rely on simpler procedures such as single-step thermal cycles. On the compositional side, both target classes cluster around three to five elements, but their distributions differ in their tails. This suggests that different property objectives favor different degrees of chemical complexity.

Together, these results confirm that GAN inversion supports both accurate property targeting and exploration of meaningful design strategies.

3.4. Experimental Validation of GAN inversion Designed Alloys

We further adopt a dual target design combined with experimental verification to verify the effectiveness of GAN inversion. Our target is set at M_s equal to 400 °C and workout equal to 10 J/cm³, it is an advanced level of high-temperature shape memory alloys. We first evaluate the effectiveness of the GAN inversion in reducing design error. As shown in [Figure 5a](#), the distribution of prediction loss, quantified as the mean squared error between predicted and target properties, is sharply and tall skewed toward lower values for GAN-optimized designs (orange) compared to randomly sampled seeds (navy). This demonstrates the framework’s ability to efficiently locate high-quality candidates within the high-dimensional latent space. The inset schematic illustrates the minimization objective in the M_s –workout plane.

Following removal of duplicate candidates from alloys designed by GAN inversion that met the target, 97 distinct alloy candidates were retained ([Supplementary Information Table S5](#)). Dimensionality reduction analysis using t-SNE ([Figure 5b](#)) revealed the design space encompasses seven alloys systems: Ti-Ni-Pd, Ti-Ni-Cu-Pd, Ni-Ti-Hf, Ni-Ti-Hf-Cu, Ni-Ti-Hf-Zr, Ni-Ti-Hf-Ta, and Ni-Ti-Hf-Cu-Ta. This outcome supports the framework’s

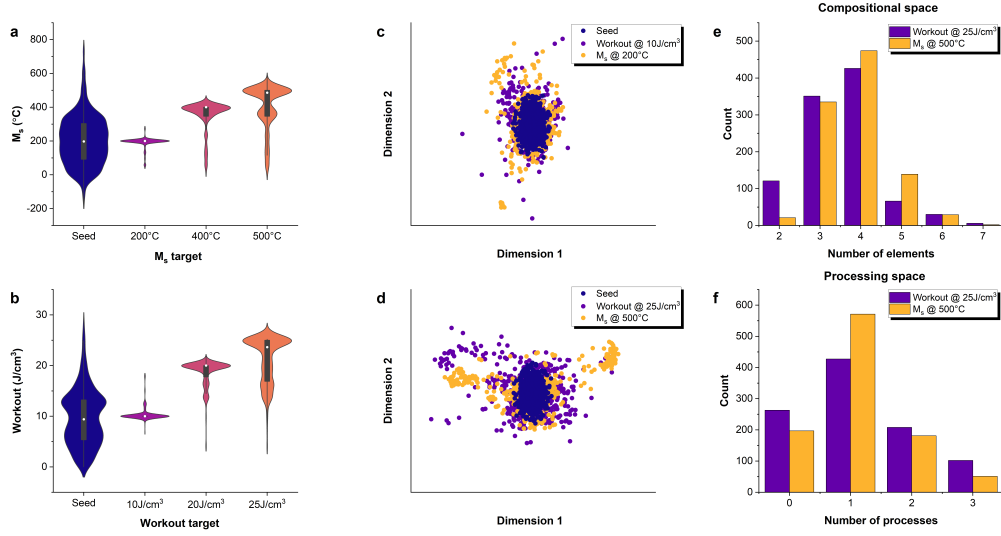


Figure 4: Property-targeted conditional generation: precise, novel, and diverse designs produced via GAN inversion. (a–b). Violin plots of generated samples targeting (a) martensite start temperature ($M_s = 200, 400, 500$ °C) and (b) mechanical work output (10, 20, 25 J/cm³). The narrowing of distributions and alignment of medians with target values demonstrate precise property control, in contrast to the broad baseline distributions of the initial seeds. (c–d). Principal component analysis (PCA) projections comparing seed samples with inversion-generated designs for distinct objectives. (c) Designs targeting $M_s = 200$ °C and workout = 10 J/cm³ show clear directional shifts in design space. (d) Designs optimized for more extreme targets ($M_s = 500$ °C, workout = 25 J/cm³) diverge further from the seed distribution, indicating exploration of novel regions. (e–f). Histograms showing the distribution of (e) number of elements in alloy composition and (f) number of processing steps for two high-performance targets: $M_s = 500$ °C (gold) and workout = 25 J/cm³ (violet). The distinct distributions show diversity of designs in both chemical and processing space.

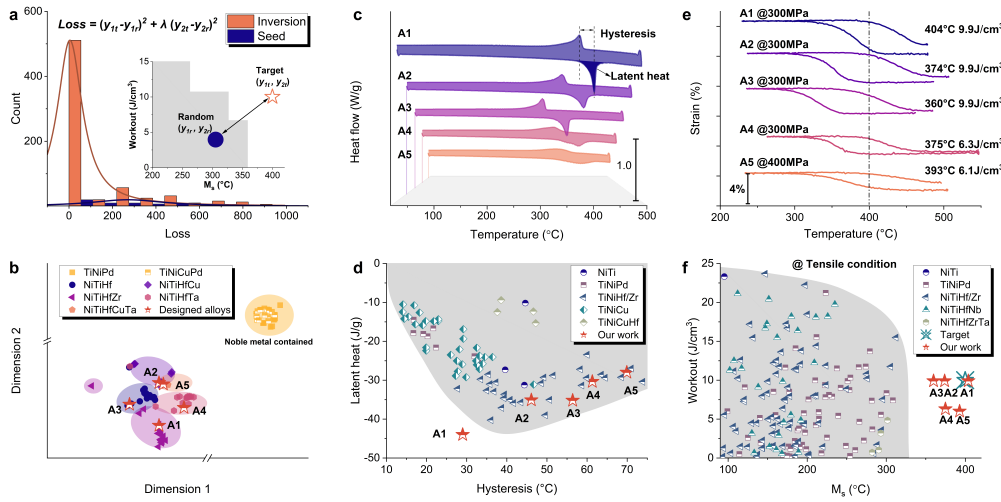


Figure 5: Experimental validation of GAN inversion-designed high-temperature shape memory alloys. (a) Distribution of loss, defined as the mean squared error between predicted and target property values, for randomly generated seed samples versus GAN-inversion-optimized candidates. Inset shows conceptual depiction of the inversion objective in the M_s –workout space. (b) t-SNE projection of alloys designed by GAN inversion that met the target in composition–processing space. Colors denote alloy families, and stars highlight the experimental validation samples. (c) DSC profiles of the five synthesized alloys (A1–A5). (d) Performance comparison of A1–A5 alloys against literature systems in the latent heat versus hysteresis space. (e) Thermomechanical characterization under applied tensile stress (300–400 MPa) between 250 °C and 510 °C. (f) Performance comparison of A1–A5 alloys against target property and literature systems mechanical workout versus M_s under tensile stress conditions.

Table 1: Composition, processing, and properties details of alloys A1–A5.

ID	Composition	Processing	Latent heat (J/g)	Hysteresis (°C)	Stress (MPa)	M_s (°C)	Workout (J/cm ³)
A1	Ni _{49.8} Ti _{26.4} Hf _{18.6} Zr _{5.2}	1000 °C 2.3 h WQ	43	29.0	300	404	9.9
A2	Ni _{46.5} Ti _{25.1} Hf _{25.2} Cu _{3.1}	830 °C 2.3 h AC	35.1	46.1	300	374	9.9
A3	Ni _{50.1} Ti _{26.6} Hf _{23.3}	630 °C 9.8 h WQ	35.2	56.4	300	360	9.9
A4	Ni _{45.5} Ti _{25.7} Hf _{24.2} Cu _{3.2} Ta _{1.4}	920 °C 2.7 h WQ	30.4	61.3	300	375	6.3
A5	Ni _{45.8} Ti _{25.7} Hf _{19.1} Zr _{2.7} Ta _{6.7}	850 °C 2.4 h WQ	28	69.9	400	393	6.1

capacity to generate chemically diverse and non-trivial designs. Considering the economic implications of precious metal constituents (Pd) in Ti-Ni-Pd and Ti-Ni-Cu-Pd systems, experimental validation was conducted on representative alloys selected from the remaining five systems.

Thermal properties of the synthesized alloys were characterized using differential scanning calorimetry (DSC), as shown in Figure 5c. All five samples exhibit clear M_s ranging from 322 to 399 °C, latent heat ranging from -28 to -43 J/g, and thermal hysteresis ranging from 29 to 69.9 °C under stress free conditions. These results indicate tunable transformation energetics enabled by alloy design. To benchmark thermodynamic efficiency, Figure 5d maps the experimental alloys in the latent heat versus hysteresis domain, alongside literature data, including NiTi [86], TiNiPd [87], TiNiHf/Zr [12, 20, 87], TiNiCu [87], TiNiCuHf [14, 88]. The GAN inversion designed alloys occupy favorable regions near the performance frontier, the alloy A1 exhibits a latent heat of 43 J/g and a thermal hysteresis of 29 °C, outperforming existing NiTi alloys, achieving a rare combination of high latent heat and reduced hysteresis.

Mechanical performance was evaluated by thermal cycling under tensile stress, as shown in Figure 5e. Alloys A1–A5 demonstrate reversible shape recovery with M_s ranging from 362 to 404 °C and mechanical workout ranging from 6.1 and 9.9 J/cm³ under 300 MPa or 400 MPa tensile stress. Alloy A1 achieved the design target with M_s of 404 °C and workout of 10J/cm³. These values place the synthesized alloys among the most effective high-temperature SMA systems reported to date.

Finally, Figure 5f situates the experimental alloys within the M_s and workout landscape along with known systems under tensile stress, including NiTi[59, 63], TiNiPd[60, 64, 65, 83], NiTiHf/Zr [55–58, 61, 62, 66, 75, 76, 78, 79], NiTiHfNb[74], NiTiHfZrTa[66]. The complete composition, processing, and properties details of alloys A1–A5 are provided in Table 1. The GAN inversion designed materials populate a previously inaccessible regime characterized by the simultaneous achievement of elevated transformation temperatures and high

mechanical work densities. This region is highly desirable for actuation applications in extreme environments.

Together, these results confirm that the GAN inversion framework can translate computational design outputs into experimentally validated, high-performance SMAs.

3.5. Crystallographic and Microstructural Basis for High Performance in Alloy A1

To elucidate the mechanisms underlying the exceptional actuation performance of Alloy A1, we conducted a detailed structural and microstructural analysis. The X-ray diffraction (XRD) patterns acquired at 300 °C and 500 °C are presented in Figure 6a. The diffraction data yielded the following lattice parameters: $a_0 = 3.1050$ Å for the B2 parent phase, and $a = 3.046$ Å, $b = 4.099$ Å, $c = 4.825$ Å, $\beta = 102.17$ ° for the B19' martensite phase. The transformation volume change was determined to be 1.66 %, which is significantly larger than those reported for Ni_{50.3}Ti₃₅Hf₂₀ and Ti_{50.1}Ni_{49.9} alloys [89]. This enhanced volume effect during phase transformation contributes to greater transformation enthalpy and high actuation strain under elevated temperatures.

Back-scattering scanning electron (BSE) microscopy image in Figure 6b reveals a uniform distribution of fine precipitates embedded within the matrix. The size distribution, quantified in Figure 6c, shows a narrow range centered around 0.75 μm. Further microstructural characterization through transmission electron microscopy (TEM) combined with selected area electron diffraction (SAED) in Figure 6d identifies the fine precipitates as cubic Ti₂Ni-type phases. Energy-dispersive X-ray spectroscopy (EDS) and scanning TEM (STEM) mapping in Figure 6e shows that the precipitates are compositionally significant enrichment of Ti and Zr, whereas Ni and Hf exhibit depletion. The accompanying line profile further quantitatively illustrates elemental segregation across the precipitate. Their relatively small size is attributed to the kinetic limitation of the diffusion of Zr and Hf during solidification due to their large atomic radius [77, 90, 91]. As the precipitates form, Hf is expelled into the surrounding matrix and Zr is extracted

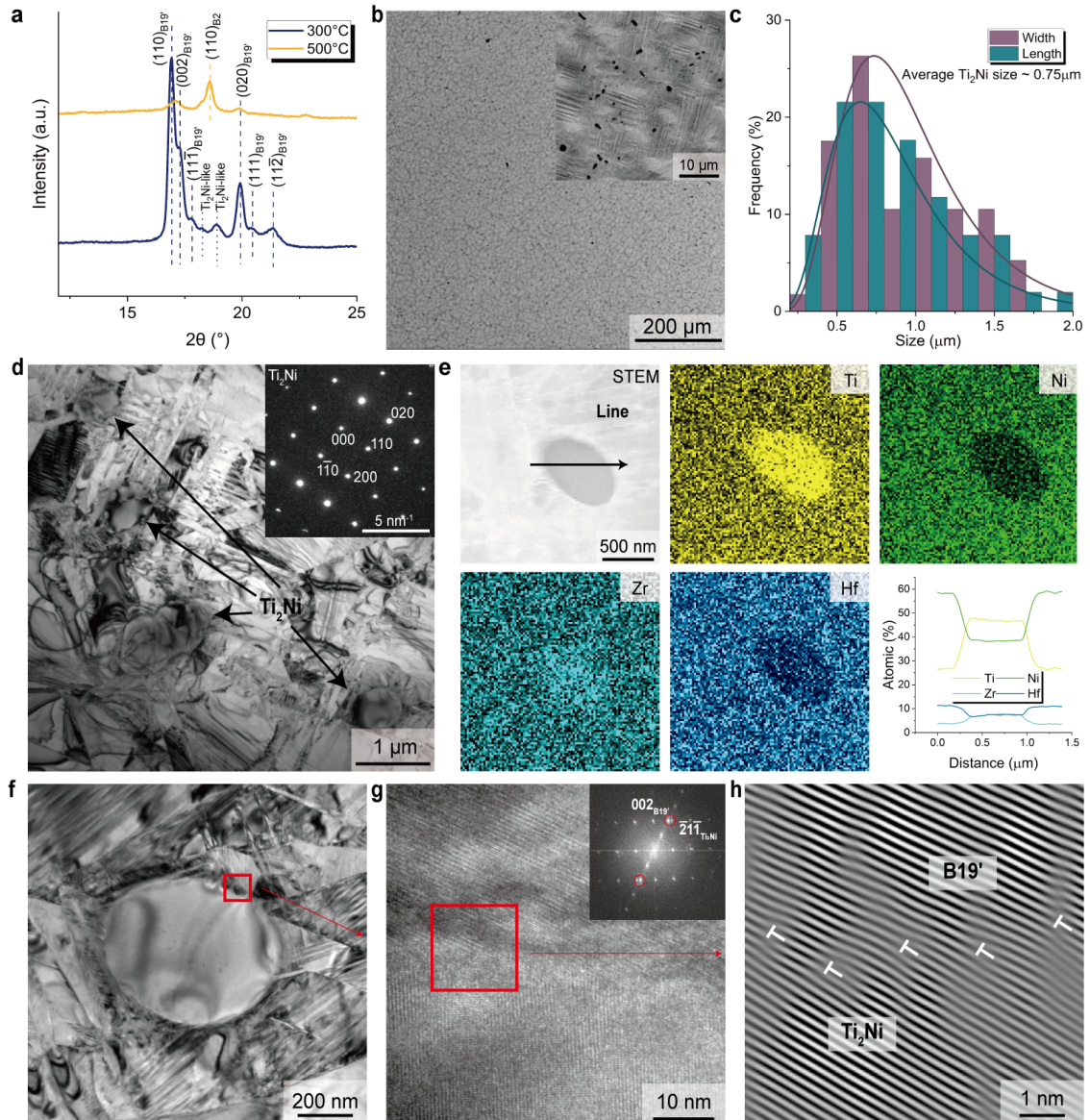


Figure 6: **Crystallographic and microstructural origin of high performance in designed Alloy A1.** (a) XRD patterns collected at 300 °C and 500 °C, indicate the presence of B19' martensite phase at 300 °C and B2 Austenite phase at 500 °C. (b) BSE image of the alloy, showing a homogenous dispersion of fine precipitates across the matrix. Inset shows a higher-magnification view. (c) Histogram of precipitate size distribution, measured along both width and length directions. (d) Bright-field TEM image shows Ti₂Ni-type precipitates in the matrix. Inset shows the corresponding SAED pattern of Ti₂Ni-type precipitate via [001] zone axis. (e) EDS elemental analysis of the Ti₂Ni-type precipitate. (f) The magnified bright field image near a Ti₂Ni-type precipitate. (g) HR-TEM of the precipitate–matrix interface. Inset shows the corresponding FFT pattern. (h) IFFT image of the red dashed area in (g) revealing local dislocations at the precipitate–matrix semi-coherent interface.

from the surrounding matrix; however, due to its sluggish diffusivity, Zr and Hf remains localized, limiting precipitate coarsening. These fine precipitates act as barriers to dislocation motion and suppress plastic deformation, thereby improving transformation reversibility under high biased stress.

Figure 6g shows a high-resolution TEM (HRTEM) image of the interface between Ti_2Ni and $\text{B19}'$ matrix (Figure 6f). The corresponding fast Fourier transformation (FFT) pattern demonstrates a semi-coherent interface, evidenced by the near-overlapping $(002)_{\text{B19}'}$ and $(\bar{2}1\bar{1})_{\text{Ti}_2\text{Ni}}$ reflections. The inverse FFT (IFFT) image of the interface region (Figure 6h) displays strained boundaries where interfacial dislocations are located. These dislocations generate localized stress fields that can lower energy barriers for transformation, thus supporting transformation reversibility and reducing thermal hysteresis [92–94]. In summary, Alloy A1 benefits from a synergistic combination of large transformation volume change, dense Ti_2Ni precipitates with strained boundaries. These features collectively contribute to its large latent heat, reduced hysteresis, and superior mechanical work output at elevated temperatures.

4. Conclusion

We have introduced a generative inversion framework for the inverse design of shape memory alloys (SMAs), enabling property-targeted generation of alloy compositions and processing conditions. By coupling a pre-trained generative adversarial network (GAN) with a differentiable property predictor, the framework performs gradient-based optimization in latent space to identify alloy designs that meet user-defined objectives, such as elevated transformation temperature and high mechanical work output.

The effectiveness of the approach was demonstrated through both computational evaluation and experimental validation. The generator successfully captured the complex, multimodal distribution of the SMA design space, while the surrogate model reliably predicted key thermo-mechanical properties. Latent space optimization enabled rapid and accurate convergence to specified property targets, producing candidate alloys with high fidelity and diversity. Among five synthesized designs, $\text{Ni}_{49.8}\text{Ti}_{26.4}\text{Hf}_{18.6}\text{Zr}_{5.2}$ achieved a martensite start temperature of $404\text{ }^\circ\text{C}$ and a mechanical work output of 9.9 J/cm^3 , a transformation enthalpy of 43 J/g , and a thermal hysteresis of $29\text{ }^\circ\text{C}$, representing a new benchmark in high-temperature SMA performance. Crystallographic and microstructural analyzes revealed that large transformation volume change, finely dispersed Ti_2Ni -type

precipitates, and semi-coherent interfaces with localized strain fields together enable large latent heat, reduced hysteresis, and superior mechanical work output at elevated temperatures.

Beyond SMAs, the proposed generative inversion strategy offers a broadly applicable framework for inverse design in complex materials systems, including high-entropy alloys and functional ceramics. By enabling targeted exploration of high-dimensional design spaces, this approach provides a powerful tool for accelerating the discovery of advanced materials.

Acknowledgements

The authors gratefully acknowledge the support of National Key Research and Development Program of China (2021YFB3802100), National Natural Science Foundation of China (Nos. 52173228, 52271190, and 524B2165), Innovation Capability Support Program of Shaanxi (2024ZG-GCZX-01(1)-06) and Natural Science Foundation Project of Shaanxi Province (Grant No. 2022JM-205).

Code and data availability

The code and data are available at <https://github.com/mil-licheng/Generative-Inversion-for-Property-Targeted-Materials-Design-Application-to-Shape-Memory-Alloys>.

References

- [1] K. Otsuka, X. Ren, [Physical metallurgy of Ti-Ni-based shape memory alloys](#), *Progress in Materials Science* 50 (5) (2005) 511–678.
- [2] M. H. Elahinia, M. Hashemi, M. Tabesh, S. B. Bhaduri, [Manufacturing and processing of NiTi implants: A review](#), *Progress in Materials Science* 57 (5) (2012) 911–946.
- [3] J. Mohd Jani, M. Leary, A. Subic, M. A. Gibson, [A review of shape memory alloy research, applications and opportunities](#), *Materials & Design* (1980-2015) 56 (2014) 1078–1113.
- [4] S. Saedi, E. Acar, H. Raji, S. E. Saghaian, M. Mirsayar, [Energy damping in shape memory alloys: A review](#), *Journal of Alloys and Compounds* 956 (2023) 170286.
- [5] J. Ma, I. Karaman, R. D. Noebe, [High temperature shape memory alloys](#), *International Materials Reviews* 55 (5) (2013) 257–315.
- [6] A. V. Shuitcev, Q. Z. Li, M. G. Khomutov, L. Li, Y. X. Tong, [Ultra-high temperature shape memory in high-Hf content NiTiHf alloys](#), *Journal of Materials Science & Technology* 209 (2025) 124–127.
- [7] Y. Tong, A. Shuitcev, Y. Zheng, [Recent Development of TiNi-Based Shape Memory Alloys with High Cycle Stability and High Transformation Temperature](#), *Advanced Engineering Materials* 22 (4) (2020).

- [8] A. Amadi, M. Mohyaldinn, S. Ridha, V. Ola, **Advancing engineering frontiers with NiTi shape memory alloys: A multifaceted review of properties, fabrication, and application potentials**, *Journal of Alloys and Compounds* 976 (2024) 173227.
- [9] C. Oses, C. Toher, S. Curtarolo, **High-entropy ceramics**, *Nature Reviews Materials* 5 (4) (2020) 295–309.
- [10] G. L. W. Hart, T. Mueller, C. Toher, S. Curtarolo, **Machine learning for alloys**, *Nature Reviews Materials* 6 (8) (2021) 730–755.
- [11] J. M. Rickman, T. Lookman, S. V. Kalinin, **Materials informatics: From the atomic-level to the continuum**, *Acta Materialia* 168 (2019) 473–510.
- [12] Y. Xian, P. Dang, Y. Tian, X. Jiang, Y. Zhou, X. Ding, J. Sun, T. Lookman, D. Xue, **Compositional design of multicomponent alloys using reinforcement learning**, *Acta Materialia* 274 (2024) 120017.
- [13] S. H. Zadeh, T. D. Brown, X. Qian, I. Karaman, R. Arroyave, **A composition-based predictive model for the transformation strain of NiTi shape memory alloys**, *Acta Materialia* 289 (2025) 120861.
- [14] C. Li, Q. Liang, Y. Zhou, D. Xue, **A knowledge-based materials descriptor for compositional dependence of phase transformation in NiTi shape memory alloys**, *Materials Genome Engineering Advances* 3 (1) (2025) e72.
- [15] A. A. Catal, E. Bedir, R. Yilmaz, D. Canadinc, **Design of a NiTiHf shape memory alloy with an austenite finish temperature beyond 400 °C utilizing artificial intelligence**, *Journal of Alloys and Compounds* 904 (2022) 164135.
- [16] S. Hossein Zadeh, C. Cakirhan, D. Khatamsaz, J. Broucek, T. D. Brown, X. Qian, I. Karaman, R. Arroyave, **Data-driven study of composition-dependent phase compatibility in NiTi shape memory alloys**, *Materials & Design* 244 (2024) 113096.
- [17] E. L. Pang, G. B. Olson, C. A. Schuh, **Low-hysteresis shape-memory ceramics designed by multimode modelling**, *Nature* 610 (7932) (2022) 491–495.
- [18] D. Xue, D. Xue, R. Yuan, Y. Zhou, P. V. Balachandran, X. Ding, J. Sun, T. Lookman, **An informatics approach to transformation temperatures of NiTi-based shape memory alloys**, *Acta Materialia* 125 (2017) 532–541.
- [19] J. Broucek, D. Khatamsaz, C. Cakirhan, S. H. Zadeh, M. Fan, G. Vazquez, K. C. Atli, X. Qian, R. Arroyave, I. Karaman, **Design of high-temperature NiTiCuHf shape memory alloys with minimum thermal hysteresis using Bayesian optimization**, *Acta Materialia* 286 (2025) 120651.
- [20] Y. Tian, B. Hu, P. Dang, J. Pang, Y. Zhou, D. Xue, **Noise-Aware Active Learning to Develop High-Temperature Shape Memory Alloys with Large Latent Heat**, *Advanced Science* (2024).
- [21] Y. Wang, P. Dang, Y. Xian, Y. Zhou, X. Ding, J. Sun, D. Xue, **Uncertainty-aware multi-objective optimization for high work output and low hysteresis in TiNiCuHfCo shape memory alloys**, *Journal of Materials Science & Technology* (2025).
- [22] D. Xue, P. V. Balachandran, J. Hogden, J. Theiler, D. Xue, T. Lookman, **Accelerated search for materials with targeted properties by adaptive design**, *Nat Commun* 7 (2016) 11241.
- [23] Y. Tian, T. Li, J. Pang, Y. Zhou, D. Xue, X. Ding, T. Lookman, **Materials design with target-oriented Bayesian optimization**, *npj Computational Materials* 11 (1) (2025) 209.
- [24] D. Canadinc, E. J. Breibach, A. A. Catal, **Characterization of Two Novel NiTiHf Shape Memory Alloys Designed by Machine Learning Utilizing Novel Experimental Techniques**, *Shape Memory and Superelasticity* (2025).
- [25] B. Shi, T. Lookman, D. Xue, **Multi-objective optimization and its application in materials science**, *Materials Genome Engineering Advances* 1 (2) (2023) e14.
- [26] L. Ding, Y. Zhou, Y. Xu, P. Dang, X. Ding, J. Sun, T. Lookman, D. Xue, **Learning from superelasticity data to search for Ti-Ni alloys with large elastocaloric effect**, *Acta Materialia* 218 (2021) 117200.
- [27] C. Zeni, R. Pinsler, D. Zügner, A. Fowler, M. Horton, X. Fu, Z. Wang, A. Shysheya, J. Crabbé, S. Ueda, R. Sordillo, L. Sun, J. Smith, B. Nguyen, H. Schulz, S. Lewis, C.-W. Huang, Z. Lu, Y. Zhou, H. Yang, H. Hao, J. Li, C. Yang, W. Li, R. Tomioka, T. Xie, **A generative model for inorganic materials design**, *Nature* 639 (8055) (2025) 624–632.
- [28] J. Wu, L. Torresi, M. Hu, P. Reiser, J. Zhang, J. S. Rocha-Ortiz, L. Wang, Z. Xie, K. Zhang, B.-w. Park, A. Barabash, Y. Zhao, J. Luo, Y. Wang, L. Lüer, L.-L. Deng, J. A. Hauch, D. M. Guldi, M. E. Pérez-Ojeda, S. I. Seok, P. Friederich, C. J. Brabec, **Inverse design workflow discovers hole-transport materials tailored for perovskite solar cells**, *Science* 386 (6727) (2024) 1256–1264.
- [29] B. Sanchez-Lengeling, A. Aspuru-Guzik, **Inverse molecular design using machine learning: Generative models for matter engineering**, *Science* 361 (6400) (2018) 360–365.
- [30] S. Lu, Q. Zhou, X. Chen, Z. Song, J. Wang, **Inverse design with deep generative models: next step in materials discovery**, *Natl Sci Rev* 9 (8) (2022) nwac111.
- [31] C. Cleeton, L. Sarkisov, **Inverse design of metal-organic frameworks using deep dreaming approaches**, *Nature Communications* 16 (1) (2025) 4806.
- [32] D. P. Kingma, M. Welling, **Auto-Encoding Variational Bayes** (December 01, 2013 2013). doi:10.48550/arXiv.1312.6114.
- [33] I. J. Goodfellow, J. Pouget-Abadie, M. Mirza, B. Xu, D. Warde-Farley, S. Ozair, A. Courville, Y. Bengio, **Generative Adversarial Networks** (June 01, 2014 2014). doi:10.48550/arXiv.1406.2661.
- [34] Z. Rao, P.-Y. Tung, R. Xie, Y. Wei, H. Zhang, A. Ferrari, T. Klaver, F. Körmann, P. T. Sukumar, A. Kwiatkowski da Silva, et al., **Machine learning-enabled high-entropy alloy discovery**, *Science* 378 (6615) (2022) 78–85.
- [35] A. Roy, A. Hussain, P. Sharma, G. Balasubramanian, M. F. N. Taufique, R. Devanathan, P. Singh, D. D. Johnson, **Rapid discovery of high hardness multi-principal-element alloys using a generative adversarial network model**, *Acta Materialia* 257 (2023) 119177.
- [36] C.-Y. Lee, C.-Y. Jui, A.-C. Yeh, Y.-J. Chang, W.-J. Lee, **Inverse design of high entropy alloys using a deep interpretable scheme for materials attribution analysis**, *Journal of Alloys and Compounds* 976 (2024) 173144.
- [37] Z. Q. Chen, Y. H. Shang, X. D. Liu, Y. Yang, **Accelerated discovery of eutectic compositionally complex alloys by generative machine learning**, *npj Computational Materials* 10 (1) (2024) 204.
- [38] X. Qin, Q. Wang, X. Zhao, S. Xia, L. Wang, Y. Zhang, C. He, D. Chen, B. Jiang, **PCS: Property-composition-structure chain in Mg-Nd alloys through integrating sigmoid fitting and conditional generative adversarial network modeling**, *Scripta Materialia* 265 (2025) 116762.
- [39] Z. Cao, Q. Liu, Q. Liu, X. Yu, J. J. Kruzic, X. Li, **A machine learning method to quantitatively predict alpha phase morphology in additively manufactured Ti-6Al-4V**, *npj Computational Materials* 9 (1) (2023) 195.
- [40] B. Peng, Y. Wei, Y. Qin, J. Dai, Y. Li, A. Liu, Y. Tian, L. Han, Y. Zheng, P. Wen, **Machine learning-enabled constrained multi-objective design of architected materials**, *Nature Communications* 14 (1) (2023) 6630.
- [41] Z. Li, N. Birbilis, **NSGAN: a non-dominant sorting optimisation-based generative adversarial design framework for alloy discovery**, *npj Computational Materials* 10 (1) (2024) 112.
- [42] J. Cai, M. Han, X. Yan, Y. Chen, D. Li, K. Zhao, D. Zhang, K. Hu, H. H. Sua, H. K. Jun, K. Xie, G. Liu, X. Liu, S. Liu, A

- process-synergistic active learning framework for high-strength Al-Si alloys design, *npj Computational Materials* 11 (1) (2025) 228.
- [43] Z. Zhou, Y. Shang, X. Liu, Y. Yang, A generative deep learning framework for inverse design of compositionally complex bulk metallic glasses, *npj Computational Materials* 9 (1) (2023) 15.
- [44] V. Attari, D. Khatamsaz, D. Allaire, R. Arroyave, Towards inverse microstructure-centered materials design using generative phase-field modeling and deep variational autoencoders, *Acta Materialia* 259 (2023) 119204.
- [45] X. Ma, Y. Zhang, C. Wang, M. Wang, M. Huang, W. Xu, Structure-to-process modeling drives experimentally validated unified dual-phase steel, *Acta Materialia* 295 (2025) 121167.
- [46] Y. Zang, P.-S. Koutsourelakis, PSP-GEN: Stochastic inversion of the Process-Structure-Property chain in materials design through deep, generative probabilistic modeling, *Acta Materialia* 284 (2025) 120600.
- [47] K. Y. Li, L. C. Liu, L. L. Shao, J. Zhou, H. B. Ke, M. Z. Li, W. H. Wang, Generative model-based inverse design of Fe-based metallic glasses with high saturation magnetic flux density, *Journal of Alloys and Compounds* 1010 (2025) 178325.
- [48] M. Abu-Mualla, E. Crabtree, F. Michael, Y. Pan, J. Huang, Inverse Design of Alloys via Generative Algorithms: Optimization and Diffusion within Learned Latent Space, *Advanced Intelligent Discovery* (2025).
- [49] P. Dang, J. Hu, Y. Xian, C. Li, Y. Zhou, X. Ding, J. Sun, D. Xue, Elastocaloric thermal battery: Ultrahigh heat-storage capacity based on generative learning-designed phase-change alloys, *Advanced Materials* 37 (8) (2025) 2412198.
- [50] S. Bartunov, D. P. Vetrov, Fast Adaptation in Generative Models with Generative Matching Networks (December 01, 2016 2016). doi:10.48550/arXiv.1612.02192.
- [51] S. K. Hung, J. Q. Gan, Small facial image dataset augmentation using conditional GANs based on incomplete edge feature input, *PeerJ Comput Sci* 7 (2021) e760.
- [52] A. Andonian, S. Osmany, A. Cui, Y. Park, A. Jahanian, A. Torralba, D. Bau, Paint by Word (March 01, 2021 2021). doi:10.48550/arXiv.2103.10951.
- [53] I. Gulrajani, F. Ahmed, M. Arjovsky, V. Dumoulin, A. Courville, Improved Training of Wasserstein GANs (March 01, 2017 2017). doi:10.48550/arXiv.1704.00028.
- [54] M. Arjovsky, S. Chintala, L. Bottou, Wasserstein GAN (January 01, 2017 2017). doi:10.48550/arXiv.1701.07875.
- [55] P. Dang, L. Zhang, Y. Zhou, C. Li, X. Ding, J. Sun, D. Xue, Nanostructured Ti-Ni-Co Alloys Showing Shape-Memory Actuation of Large Work Output at Low Temperature, *Advanced Engineering Materials* 26 (4) (2023) 2301438.
- [56] N. Babacan, M. Bilal, C. Hayrettin, J. Liu, O. Benafan, I. Karaman, Effects of cold and warm rolling on the shape memory response of Ni₅₀Ti₃₀Hf₂₀ high-temperature shape memory alloy, *Acta Materialia* 157 (2018) 228–244.
- [57] J. Dong, A. Demblon, T. Umale, D. Zhao, G. Valentino, I. Karaman, K. Y. Xie, Property and microstructure of Ni_{50.3}Ti_{29.7}Hf₂₀ high-temperature shape memory alloys with different aging conditions, *Acta Materialia* 265 (2024) 119642.
- [58] S. Baradari, N. Resnina, S. Belyaev, M. Nili-Ahmadabadi, Martensitic phase transformation and shape memory properties of the as-cast NiCuTiHf and NiCuTiHfZr alloys, *Journal of Alloys and Compounds* 888 (2021) 161534.
- [59] C.-H. Chen, N.-H. Lu, Improved functional stability of Ti-rich TiNi shape memory ribbon prepared by melt-spinning, *Journal of Alloys and Compounds* 819 (2020) 152988.
- [60] H. Li, X. Meng, W. Cai, Shape memory behaviors in a Ti₅₀Ni_{33.5}Cu_{12.5}Pd₄ alloy with near-zero thermal hysteresis, *Journal of Alloys and Compounds* 765 (2018) 166–170.
- [61] G. S. Bigelow, A. Garg, O. Benafan, R. D. Noebe, S. A. Padula, D. J. Gaydosh, Development and testing of a Ni_{50.5}Ti_{27.2}Hf_{22.3} high temperature shape memory alloy, *Materialia* 21 (2022) 101297.
- [62] S. M. Saghaian, H. E. Karaca, M. Souri, A. S. Turabi, R. D. Noebe, Tensile shape memory behavior of Ni_{50.3}Ti_{29.7}Hf₂₀ high temperature shape memory alloys, *Materials & Design* 101 (2016) 340–345.
- [63] K. Huang, H. Yin, M. Li, Q. Sun, Grain size dependence of stress-assisted two-way memory effect in Ti-50.04 at.% Ni shape memory alloy, *Materials Science and Engineering: A* 856 (2022) 143872.
- [64] M. Imahashi, M. I. Khan, H. Y. Kim, S. Miyazaki, The effect of Pd content on microstructure and shape-memory properties of Ti-Ni-Pd-Cu alloys, *Materials Science and Engineering: A* 602 (2014) 19–24.
- [65] S. u. Rehman, M. Khan, A. Nusair Khan, L. Ali, S. Zaman, M. Waseem, L. Ali, S. H. I. Jaffery, Transformation behavior and shape memory properties of Ti₅₀Ni₁₅Pd₂₅Cu₁₀ high temperature shape memory alloy at various aging temperatures, *Materials Science and Engineering: A* 619 (2014) 171–179.
- [66] W. Tasaki, Y. Arai, S. Miyazaki, H. Y. Kim, Development of Ni-Ti-Zr-Hf-(Nb, Ta) Multi-Principal Element High-Temperature Shape Memory Alloys with High Cold Workability, *MATERIALS TRANSACTIONS* 64 (10) (2023) 2457–2465.
- [67] C.-H. Chen, Y.-J. Chen, Shape memory characteristics of (TiZrHf)₅₀Ni₂₅Co₁₀Cu₁₅ high entropy shape memory alloy, *Scripta Materialia* 162 (2019) 185–189.
- [68] J. Pang, Y. Xu, J. Tian, Y. Zhou, D. Xue, X. Ding, J. Sun, Effect of Ti/Ni and Hf/Zr ratio on the martensitic transformation behavior and shape memory effect of TiNiHfZr alloys, *Materials Science and Engineering: A* 807 (2021) 140850.
- [69] J. Pang, P. Dang, J. Tian, L. Zhang, Y. Zhou, X. Ding, J. Sun, D. Xue, Effect of Cu content on martensitic transformation and shape memory behavior in Ti_{31.5}Hf₁₅Zr₅Ni_{48.5-x}Cu_x alloys, *Journal of Materials Science* 59 (24) (2024) 11096–11109.
- [70] E. Acar, G. P. Toker, H. Kurkcu, H. E. Karaca, High temperature shape memory behavior of Ni_{47.3}Ti_{29.7}Hf₂₀Pd₃ alloys, *Intermetallics* 111 (2019) 106518.
- [71] G. P. Toker, S. Saedi, E. Acar, O. Ozbulut, H. E. Karaca, Shape memory behavior of Ni_{40.3}Ti_{39.7}Hf₁₅Pd₅ and Ni_{40.3}Ti_{44.7}Hf₁₀Pd₅ alloys, *Journal of Alloys and Compounds* 763 (2018) 1012–1017.
- [72] S. Saedi, G. P. Toker, H. Raji, E. Acar, F. Watanabe, H. Karaca, Shape Memory Effect in Quaternary NiTiHfPd Shape Memory Alloys beyond 200 °C, *Journal of Materials Engineering and Performance* 31 (8) 6689–6696.
- [73] D. Canadinc, W. Trehern, J. Ma, I. Karaman, F. Sun, Z. Chaudhry, Ultra-high temperature multi-component shape memory alloys, *Scripta Materialia* 158 (2019) 83–87.
- [74] H. Y. Kim, T. Jinguu, T.-h. Nam, S. Miyazaki, Cold workability and shape memory properties of novel Ti-Ni-Hf-Nb high-temperature shape memory alloys, *Scripta Materialia* 65 (9) (2011) 846–849.
- [75] A. Evirgen, I. Karaman, R. Santamarta, J. Pons, R. D. Noebe, Microstructural characterization and shape memory characteristics of the Ni_{50.3}Ti_{34.7}Hf₁₅ shape memory alloy, *Acta Materialia* 83 (2015) 48–60.
- [76] A. Evirgen, I. Karaman, R. D. Noebe, R. Santamarta, J. Pons, Effect of precipitation on the microstructure and the shape memory response of the Ni_{50.3}Ti_{29.7}Zr₂₀ high temperature shape memory alloy, *Scripta Materialia* 69 (5) (2013) 354–357.
- [77] H. E. Karaca, S. M. Saghaian, G. Ded, H. Tobe, B. Basaran, H. J. Maier, R. D. Noebe, Y. I. Chumlyakov, Effects of nanoprecipitation on the shape memory and material properties of an Ni-rich

- NiTiHf high temperature shape memory alloy, *Acta Materialia* 61 (19) (2013) 7422–7431.
- [78] O. Karakoc, C. Hayrettin, M. Bass, S. J. Wang, D. Canadinc, J. H. Mabe, D. C. Lagoudas, I. Karaman, [Effects of upper cycle temperature on the actuation fatigue response of NiTiHf high temperature shape memory alloys](#), *Acta Materialia* 138 (2017) 185–197.
- [79] A. Demblon, J. H. Mabe, I. Karaman, [Compositional effects on strain-controlled actuation fatigue of NiTiHf high temperature shape memory alloys](#), *Scripta Materialia* 242 (2024) 115904.
- [80] H. Chen, F. Xiao, X. Liang, Z. Li, Z. Li, X. Jin, T. Fukuda, [Giant elastocaloric effect with wide temperature window in an Al-doped nanocrystalline Ti–Ni–Cu shape memory alloy](#), *Acta Materialia* 177 (2019) 169–177.
- [81] S. M. Saghaian, H. E. Karaca, H. Tobe, A. S. Turabi, S. Saedi, S. E. Saghaian, Y. I. Chumlyakov, R. D. Noebe, [High strength NiTiHf shape memory alloys with tailorable properties](#), *Acta Materialia* 134 (2017) 211–220.
- [82] H. E. Karaca, E. Acar, G. S. Ded, S. M. Saghaian, B. Basaran, H. Tobe, M. Kok, H. J. Maier, R. D. Noebe, Y. I. Chumlyakov, [Microstructure and transformation related behaviors of a Ni_{45.3}Ti_{29.7}Hf₂₀Cu₅ high temperature shape memory alloy](#), *Materials Science and Engineering: A* 627 (2015) 82–94.
- [83] G. S. Bigelow, S. A. Padula, A. Garg, D. Gaydos, R. D. Noebe, [Characterization of Ternary NiTiPd High-Temperature Shape-Memory Alloys under Load-Biased Thermal Cycling](#), *Metallurgical and Materials Transactions A* 41 (12) (2010) 3065–3079.
- [84] P. Dang, Y. Zhou, J. Pang, X. Ding, J. Sun, T. Lookman, D. Xue, [Achieving stable actuation response and elastocaloric effect in a nanocrystalline Ti₅₀Ni₄₀Cu₁₀ alloy](#), *Scripta Materialia* 226 (2023) 115263.
- [85] A. V. Shuitcev, M. G. Khomutov, R. N. Vasin, L. Li, I. S. Golovin, Y. F. Zheng, Y. X. Tong, [The role of H-phase in thermal hysteresis and shape memory properties in Ni₅₀Ti₃₀Hf₂₀ alloy](#), *Scripta Materialia* 230 (2023) 115391.
- [86] C.-Y. Nien, H.-K. Wang, C.-H. Chen, S. Ii, S.-K. Wu, C.-H. Hsueh, [Superelasticity of TiNi-based shape memory alloys at micro/nanoscale](#), *Journal of Materials Research* 29 (22) (2014) 2717–2726.
- [87] J. Frenzel, A. Wiczorek, I. Opahle, B. Maaß, R. Drautz, G. Eggeler, [On the effect of alloy composition on martensite start temperatures and latent heats in Ni–Ti-based shape memory alloys](#), *Acta Materialia* 90 (2015) 213–231.
- [88] D. Piorunek, J. Frenzel, N. Jöns, C. Somsen, G. Eggeler, [Chemical complexity, microstructure and martensitic transformation in high entropy shape memory alloys](#), *Intermetallics* 122 (2020) 106792.
- [89] A. Shuitcev, R. N. Vasin, X. M. Fan, A. M. Balagurov, I. A. Bobrikov, L. Li, I. S. Golovin, Y. X. Tong, [Volume effect upon martensitic transformation in Ti_{29.7}Ni_{50.3}Hf₂₀ high temperature shape memory alloy](#), *Scripta Materialia* 178 (2020) 67–70.
- [90] A. Shuitcev, Y. Ren, B. Sun, G. V. Markova, L. Li, Y. X. Tong, Y. F. Zheng, [Precipitation and coarsening kinetics of H-phase in NiTiHf high temperature shape memory alloy](#), *Journal of Materials Science & Technology* 114 (2022) 90–101.
- [91] X. L. Meng, W. Cai, Y. D. Fu, J. X. Zhang, L. C. Zhao, [Martensite structure in Ti–Ni–Hf–Cu quaternary alloy ribbons containing \(Ti,Hf\)₂Ni precipitates](#), *Acta Materialia* 58 (10) (2010) 3751–3763.
- [92] Y.-T. Hsu, N.-H. Lu, Y. Kimura, R. Kainuma, C.-H. Chen, [Improving ductility and functional properties of \(TiZrHf\)₅₀Ni₂₅Co₁₀Cu₁₅ high entropy shape memory by melt-spinning technique](#), *Scripta Materialia* 259 (2025) 116557.
- [93] X. Li, Q. Liang, T. Dong, C. Liang, D. Wang, Y. Wang, X. Ding, [Fatigue-resistant elastocaloric effect in hypoeutectic TiNi₅₈ alloy with heterogeneous microstructure](#), *Acta Materialia* 262 (2024) 119464.
- [94] H. Hou, E. Simsek, T. Ma, N. S. Johnson, S. Qian, C. Cisse, D. Stasak, N. Al Hasan, L. Zhou, Y. Hwang, R. Radermacher, V. I. Levitas, M. J. Kramer, M. A. Zaem, A. P. Stebner, R. T. Ott, J. Cui, I. Takeuchi, [Fatigue-resistant high-performance elastocaloric materials made by additive manufacturing](#), *Science* 366 (6469) (2019) 1116–1121.